Available online at www.sciencedirect.com
ScienceDirect
Journal of the European Ceramic Society 27 (2007) 3191–3199
www.elsevier.com/locate/jeurceramsoc

# Microstructure evaluation of $Al_2O_3$ ceramics with Mg-PSZ- and $TiO_2$-additions

C.G. Aneziris *, W. Schärfl, B. Ullrich

*Institute of Ceramic, Glass and Construction Materials, Technical University of Freiberg, Germany*

Received 23 June 2006; received in revised form 10 January 2007; accepted 11 January 2007
Available online 26 February 2007

**Abstract**

Thermal shock improved microstructures of porous alumina fine grained materials have been obtained with Mg-PSZ- and $TiO_2$-additions. The new material displays a non-linear deformation behaviour as a function of the applied stress and presents a very low Young's modulus of elasticity. The extrusion technique has been selected in order to produce porous honeycomb structures. By the aid of a special gas burner equipment the cyclical thermal shock performance of the material has been evaluated.


*Keywords:* $Al_2O_3$; $ZrO_2$; $TiO_2$; Thermal shock resistance

## 1. Introduction

Structural $Al_2O_3$ ceramic composites prepared by the introduction of fine $ZrO_2$ particles in the alumina matrix are widely used in construction applications as well as biomaterials due to high levels of mechanical strength, toughness and hardness.[1] Hasselman has established the thermal stress resistance parameters related to the thermal expansion coefficient, the Young's modulus of elasticity, the fracture tensile stress and the thermal conductivity. He has illustrated the effect of thermal shock on the strength of ceramics and the regions of applicability (resistance to fracture, loss in strength due to fracture and crack stability followed by further weakening) of the various thermal stress fracture parameters. A low thermal expansion coefficient and a low Young's modulus of elasticity improve the thermal shock performance.[2,3] The combination of $Al_2O_3$ and $TiO_2$ leads to the formation of $Al_2TiO_5$ that exhibits the highest $R_1$ thermal shock parameter according to Hasselman among all other ceramics.[4] $Al_2TiO_5$ ceramics have a very low thermal expansion because of micro-cracks at grain boundaries induced by the high anisotropy along its three crystallographic axes.[5] However, pure $Al_2TiO_5$ tends to decompose into $Al_2O_3$ and $TiO_2$ at temperatures ranging from 800 to 1300 °C during cooling as a result of eutectic reactions.[6] Following decomposition, the material no longer exhibits either a low thermal expansion coefficient or favourable thermal shock behaviour.[7] The thermal durability of $Al_2TiO_5$ can be improved by the formation of solid solutions with MgO, $Fe_2O_3$ or $TiO_2$ which are isomorphous with the mineral pseudobrookite.[8] Another source of stabilisation is the limitation of micro-cracks, micro-cracks growth as well as grain growth by the addition of additives such as $SiO_2$, $ZrO_2$, $ZrTiO_4$ or Mullite most of which do not form a solid solution with $Al_2TiO_5$ but rather restrain the tendency of $Al_2TiO_5$ towards decomposition.[9] Especially during sintering of $Al_2TiO_5$–$ZrTiO_4$-mixtures composite materials with high temperature stability as well as low thermal coefficient can be produced due to in situ partial reactions.[10] Unfortunately under thermal shock cycling a partially decomposition of such materials is also observed due to micro-crack growth.[11]

The production of tetragonal zirconia polycrystalline ceramics and the identification of factors controlling retention of the tetragonal phase in the $ZrO_2$–$TiO_2$ system have been investigated by Pandolfelli and Rodrigues.[12] In solid solution, $TiO_2$ additions to $ZrO_2$ act to suppress the densification of $ZrO_2$, leading to grain growth when attempts are made to attain higher densities. The use of fine powders and fast firing techniques are not able to keep the final grain size of $ZrO_2$ small enough to avoid spontaneous tetragonal to monoclinic transformation during cooling. Osendi and Moya showed in the past in a

* Corresponding author.
*E-mail address:* aneziris@ikgb.tu-freiberg.de (C.G. Aneziris).

0955-2219/$ – see front matter © 2007 Elsevier Ltd. All rights reserved.
doi:10.1016/j.jeurceramsoc.2007.01.006

$Al_2O_3$–8 vol.% $ZrO_2$ composite, that although $TiO_2$ additions cause the initial sintering rate of the composite to increase, a significant enhancement of the grain growth kinetics of $ZrO_2$ is observed after annealing.[13]

A very interesting approach to study the thermal expansion behaviour of ceramic composites in the system $Al_2O_3$–$ZrO_2$–$TiO_2$ has been presented by Virro-Nic and Pilling.[14] Compositions were prepared from blended mixtures of oxide powders ($Al_2O_3$, Aldrich, purity 99.8%, particle size <10 μm; $TiO_2$, Johnson–Matthey, purity >99%, particle size 1.5–2.0 μm; $ZrO_2$, Johnson–Matthey, purity >99%, −325 mesh) which were compacted into cylindrical rods and then melted in a tungsten arc-image furnace. They demonstrated that compositions of 20 mol% $Al_2O_3$, 20 mol% $ZrO_2$ and 60 mol% $TiO_2$ present a thermal expansion coefficient of $-4.18 \times 10^{-6}\,K^{-1}$. A composition based on 40 mol% $TiO_2$, 40 mol% $ZrO_2$ and 20 mol% $Al_2O_3$ reaches a thermal expansion coefficient of $0.5 \times 10^{-6}\,K^{-1}$, whereby 100 mol% $Al_2O_3$ presents a thermal expansion coefficient of $8.6 \times 10^{-6}\,K^{-1}$, 100 mol% $ZrTiO_4$ of $7.3 \times 10^{-6}$ and 100 mol% $Al_2TiO_5$ of $-3.5 \times 10^{-6}\,K^{-1}$.

In a previous work fine grained Mg-PSZ ceramics with titania and alumina additions are investigated.[15] Through the addition of $TiO_2$ and $Al_2O_3$ a high amount of the tetragonal phase is transformed and the monoclinic phase is being increased. $TiO_2$ is incorporated in the zirconia lattice and a part of the MgO stabilising agent is removed from the zirconia cell and reacts with the $Al_2O_3$ to give $MgAl_2O_4$. Through the loss of the stabilising agent martensitic phase transformation occurs. Due to the martensitic transformation as well as the spinel formation a micro-crack pattern is generated that leads to low thermal expansion coefficient as well as low Young's modulus of elasticity. Both parameters with their low values contribute to the thermal shock performance of fine grained Mg-PSZ ceramics.

Main task of this work is to improve the thermal shock behaviour as well as the thermal cyclic stability of fine grained porous alumina based materials due to Mg-PSZ (magnesia partial stabilized zirconia) and $TiO_2$-additions.

The regulations regarding automotive diesel engine emissions become more severe every day, and it is difficult to meet the requirements with only combustion improvement techniques or exhaust gas recirculation. More effective after treatment technology is desired, especially for particulate matter, such as carbon soots. The use of ceramic diesel particulate filter is now a leading technology for particulate matter removal and honeycombs made from SiC have been widely used for the collection of carbon soot.[16,17] A thermal shock resistant fine grained porous alumina material exhibits at least the same corrosion resistance as SiC in diesel exhaust gas environments and is a promising low cost alternative for diesel exhaust gas filters in comparison to the commercial available SiC-materials.[18]

## 2. Experimental

The extrusion technique has been selected as the most suitable processing route to form honeycombs and rods. The plastic feed material based on the compositions listed in Table 1 is prepared by directly batching and mixing the raw materials in a high-shear auger mixer. In a further step the plasticizers and water have been added to the batch during mixing in a conventional baking mixer. Due to a piston extruder honeycombs 23.5 mm × 23.5 mm with 196 channels and wall thickness of 250 μm as well as full round rods with a diameter of 5 mm have been extruded. The applied pressure was lying between 10 MPa for the honeycombs and 9.5 MPa for the strands. The samples have been dried at 40 °C for 6 h (humidity 80%) and at 90 °C for 6 h (humidity 5%) in an air circulated dryer. Samples have then been sintered at 1500 °C (Material AZT 1500) and at 1600 °C (Material AZT 1600 and Material AL 1600) for 2 h at the maximum temperature in an electrical furnace with sintering curves obtained from dilatometer curves. The obtained microstructures have been characterised by scanning electron microscope (SEM), electron dispersive X-ray (EDX) analysis as well as electron backscatter diffraction (EBSD) techniques. Using X-ray diffraction the phase evolution of the different sintered materials has been identified.

Table 1
Composition of mixtures

| Recipe | | | AZT (wt.%) | AL (wt.%) |
|---|---|---|---|---|
| Material | Type | Supplier | | |
| Inorganic raw materials | | | | |
| $Al_2O_3$ | T60, $d_{50} = 55$ μm | Almatis | 29.76 | 33.44 |
| $Al_2O_3$ | CTC9 FG, $d_{50} = 4$ μm | Almatis | 43.29 | 43.29 |
| $TiO_2$ | Tronox TR, $d_{50} = 1$ μm | Kerr | 1.84 | – |
| $ZrO_2$ with 3.5 wt.% MgO | PMG3.5, $d_{50} = 2$ μm | Unitec | 1.84 | – |
| Pore former | | | | |
| Flour | HW FGB $d_{50} = 55$ μm | Kampffmeyer | 10.82 | 10.82 |
| Acrylate | Porlat K86 $d_{50} = 130$ μm | Z&S | 8.12 | 8.12 |
| Organic additives | | | | |
| Casterment FS 10 | Degussa | 0.54 | 0.54 | |
| Tenside | Henkel | 1.62 | 1.62 | |
| Culminal 6000 PR | Aqualon | 2.15 | 2.15 | |
| Plus additional water | | | | |
| Water | | | 16.77 | 16.22 |

The density and porosity of sintered samples were measured by Archimedes principle as well as the distribution of the porosity due to mercury porosimetry. Samples out of the rods (5 mm in diameter × 45 mm in length) and honeycombs 20 mm × 20 mm × 150 mm with 196 channels (higher number of channels per area due to shrinkage after sintering) have been used for the evaluation of the mechanical properties. In each case 20 samples for three point – bending strength – tests of dried as well as sintered samples were measured as fired at room temperature according to EN 843. In addition four point bending strengths were measured at room temperature after quenching special honeycomb samples (4 mm × 6 mm × 45 mm with 12 channels) in water from 200, 400 to 600 °C. Beside this thermal shock test, honeycomb samples as described before have been shocked thermally by a special gas burner construction (power 2500 W) for 1000 cycles. The shocking cyclic profile was heating with 800 K/min and cooling with 400 K/min. After the burner thermal shock test residual three point bending strengths have been also measured according to EN 843. In a further step the thermal expansion (honeycomb sample 4 mm × 6 mm × 45 mm with 12 channels) in a horizontal Netsch Dilatometer and the static Young's modulus of elasticity due to three point bending strength tests of the honeycomb samples as well as of the rod samples have been measured.

## 3. Results and discussion

### 3.1. Microstructure and phase evolution

Fig. 1 presents honeycombs as pressed as well as fired. Due to the additions of $TiO_2$ and Mg-PSZ in $Al_2O_3$ (Material AZT 1500 and Material AZT 1600) a higher shrinkage is observed in comparison to the pure $Al_2O_3$ Material AL 1600. The shrinkage after firing reaches a value of 14.9% for AZT 1600, 14.1% for AZT 1500 and 10.6% for AL 1600.

Fig. 2 presents the micro-porosity as well as macro-porosity incorporated in the thin wall matrix of AZT 1600 due to organic and inorganic pore formers. The water, the flour, the acrylate as well as the plasticizers contribute to the porosity. In addition, in situ formed micro-cracks during sintering and cooling-down increase the porosity in Material AZT 1600. In Table 2 the porosities and the main pore sizes of the three materials are listed.

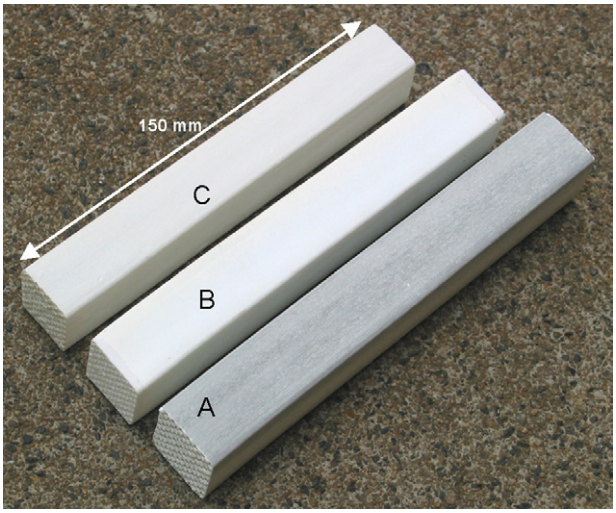


Fig. 1. Honeycombs: (A) as pressed, (B) Material AL 1600 as fired and (C) Material AZT 1600 as fired.

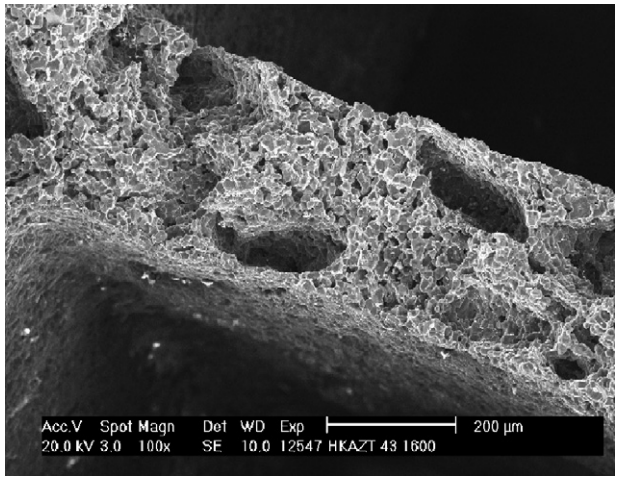


Fig. 2. Surface of Material AZT 1600, SEM micrograph, macro- and micro-porosity.

Table 2
Porosities and pore sizes

| | AL 1600 | AZT 1500 | AZT 1600 |
|---|---|---|---|
| Open porosity (%) | 36 | 43 | 42 |
| $d_{10}$ (µm) | 0.7 | 3.1 | 3.0 |
| $d_{50}$ (µm) | 2.5 | 4.9 | 4.8 |
| $d_{90}$ (µm) | 12 | 18.5 | 17.0 |

The addition of $TiO_2$ and Mg-PSZ leads to higher shrinkages but also contributes to grain growth, Fig. 3 microstructure of AL 1600 and Fig. 4 microstructure of AZT 1600.

In Fig. 5 a well distributed white phase can be identified in Material AZT 1600. In a higher magnification (Fig. 6) besides $Al_2O_3$ grains three additional zones can be identified. According to EDX-analysis zone 1 is a $ZrO_2$-rich area (white phase in Fig. 6) with less than 0.5 wt.% MgO stabilising agent,

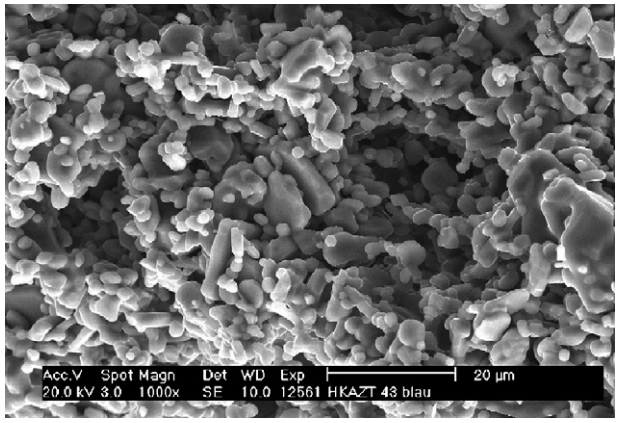


Fig. 3. Microstructure of the surface of Material AL 1600, SEM micrograph.

Table 3
EDX analysis of Mg-PSZ starting powder as well as the $ZrO_2$-rich area (zone 1) of Materials AZT 1500 and AZT 1600

| Material | $ZrO_2$ | | MgO | | $TiO_2$ | | $Al_2O_3$ | |
|---|---|---|---|---|---|---|---|---|
| | wt.% | mol% | wt.% | mol% | wt.% | mol% | wt.% | mol% |
| $ZrO_2$ powder | 95.42 | 88.24 | 3.88 | 10.97 | – | – | 0.70 | 0.78 |
| Zone 1 | | | | | | | | |
| AZT 1500 | 90.17 | 85.72 | 0.31 | 0.89 | 7.27 | 10.65 | 2.07 | 2.38 |
| AZT 1600 | 87.95 | 82.27 | 0.19 | 0.53 | 8.29 | 11.96 | 2.05 | 2.32 |

Table 4
EDX analysis of the $TiO_2$-rich area (zone 2) of Materials AZT 1500 and AZT 1600

| Material | $ZrO_2$ | | MgO | | $TiO_2$ | | $Al_2O_3$ | |
|---|---|---|---|---|---|---|---|---|
| | wt.% | mol% | wt.% | mol% | wt.% | mol% | wt.% | mol% |
| AZT 1500 | 18.05 | 12.78 | 0.14 | 0.30 | 65.57 | 71.61 | 13.71 | 11.73 |
| AZT 1600 | 35.39 | 27.35 | 0.11 | 0.26 | 44.65 | 53.21 | 18.82 | 17.58 |

Table 5
EDX analysis of the $ZrO_2$–$TiO_2$–$Al_2O_3$-rich area (zone 3) of Materials AZT 1500 and AZT 1600

| Material | $ZrO_2$ | | MgO | | $TiO_2$ | | $Al_2O_3$ | |
|---|---|---|---|---|---|---|---|---|
| | wt.% | mol% | wt.% | mol% | wt.% | mol% | wt.% | mol% |
| AZT 1500 | 28.84 | 21.89 | 0.65 | 1.51 | 28.15 | 32.95 | 35.51 | 32.57 |
| AZT 1600 | 34.79 | 26.14 | 0.58 | 1.33 | 33.44 | 38.75 | 23.27 | 21.12 |

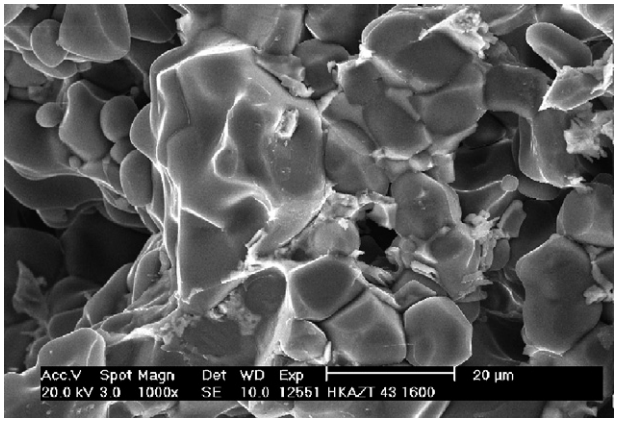


Fig. 4. Microstructure of the surface of Material AZT 1600, SEM micrograph, magnification 1000×.

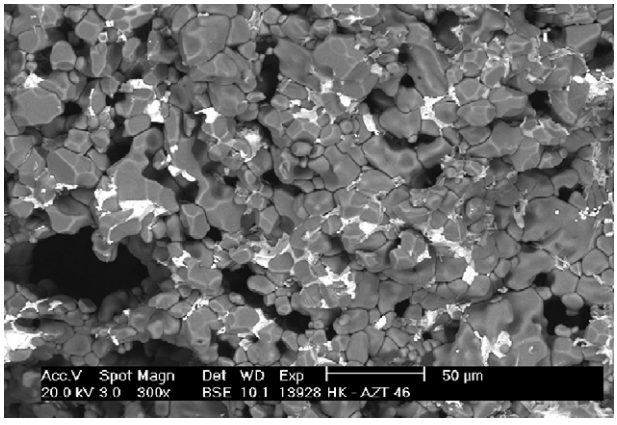


Fig. 5. Microstructure of the surface of Material AZT 1600, SEM micrograph, magnification 300×.

zone 2 is a $TiO_2$-rich area (light grey phase in Fig. 6) and zone 3 is a $ZrO_2$–$TiO_2$–$Al_2O_3$-rich area (dark grey phase in Fig. 6), Tables 3–5. In addition in zone 3 in several samples Ca due to EDX has been identified, approximately equivalent to 5.28 wt.% or 8.72 mol% CaO. Due to a précise chemical analysis this CaO has been identified as an impurity (approximately 0.3 wt.%) in the tabular $Al_2O_3$ starting powder. The XRD micro-structural characterization identified besides Corundum

Table 6
EDX analysis of the $Al_2TiO_5$-rich area (zone 4) in Material AZT 1500

| Material | $ZrO_2$ | | MgO | | $TiO_2$ | | $Al_2O_3$ | |
|---|---|---|---|---|---|---|---|---|
| | wt.% | mol% | wt.% | mol% | wt.% | mol% | wt.% | mol% |
| $Al_2TiO_5$ | | | | | | | | |
| AZT 1500 | – | – | – | – | 47.15 | 50.60 | 41.93 | 35.27 |
| AZT 1600 | – | – | – | – | – | – | – | – |

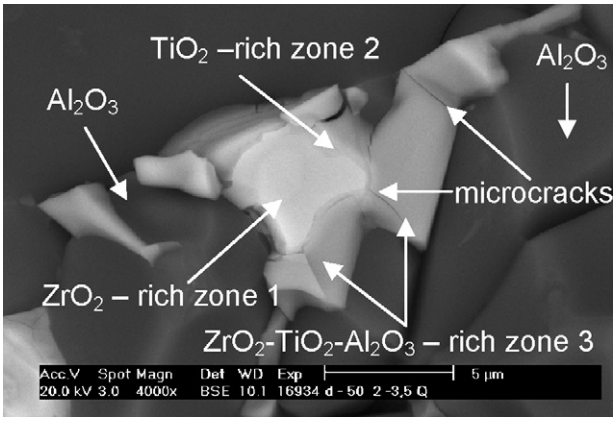


Fig. 6. Microstructure of the surface of Material AZT 1600, SEM micrograph, magnification 4000×.

Baddelyte, $ZrTiO_4$ and $CaZrTi_2O_7$. The same phases due to XRD as well as similar elements have been identified in Material AZT 1500 sintered at 1500 °C. In addition $Al_2TiO_5$ has been registered due to XRD. Fig. 7 presents the microstructure of AZT 1500. Besides the zones 1–3 an $Al_2TiO_5$-rich area (zone 4) has been identified; Figs. 7 and 8, Table 6. Both Materials AZT 1500 and AZT 1600 present micro-cracks in zone 3. This $ZrO_2$–$TiO_2$–$Al_2O_3$-rich area seems to be a recrystallized melt and contributes as "glue" between the $Al_2O_3$ grains.

### 3.2. Mechanical and thermal properties

In Fig. 9 the curves of the three point bending strength tests of the honeycombs based on Materials AZT 1500 and AZT 1600 are plotted. Both materials present non-linear deformation behaviour as a function of the applied stress. Fig. 10 presents the three point bending strength results of rods and honeycombs based on Material AZT 1600 and in Fig. 11 the bending strengths of rods based on both materials. Surprisingly the high temperature material fired at 1600 °C (AZT 1600) achieves a lower strength than the material fired at 1500 °C.

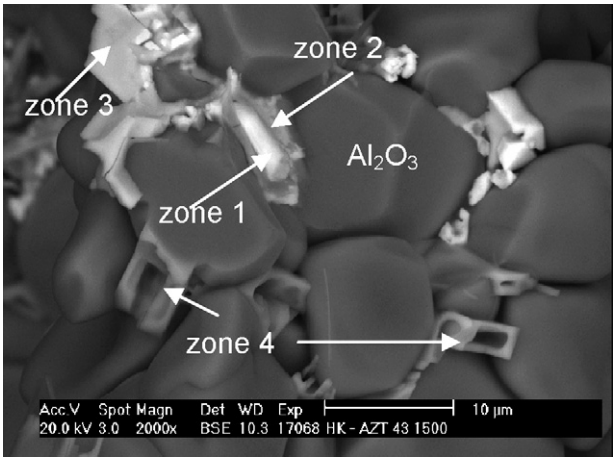


Fig. 7. Microstructure of the surface of Material AZT 1500, SEM micrograph, magnification 2000×.

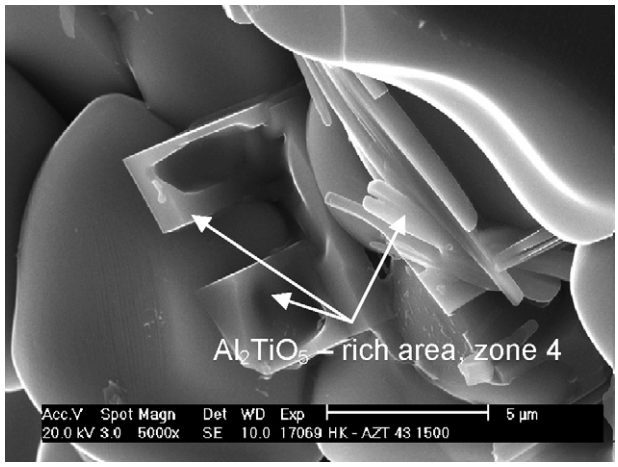


Fig. 8. Microstructure of the surface of Material AZT 1500, SEM micrograph, magnification 5000×.

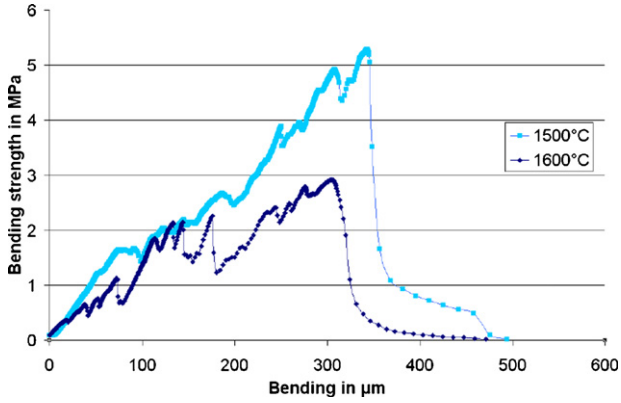


Fig. 9. Three point bending strength tests of honeycombs based on the Materials AZT 1500 and AZT 1600.

In Table 7 the mechanical properties of the Materials AL 1600, AZT 1500 and AZT 1600 are demonstrated based on rod as well as on honeycomb specimens.

Material AZT 1600 as a full rod structure with approximately 42 vol.% porosity presents a very low Young's modulus of elasticity of 8.5 GPa. In comparison to $Al_2TiO_5$[4] (starting powder type electrofused ATG 6, grain size <10 μm, samples slip casted and sintered at 1450 °C) 70% less Young' modulus of elasticity

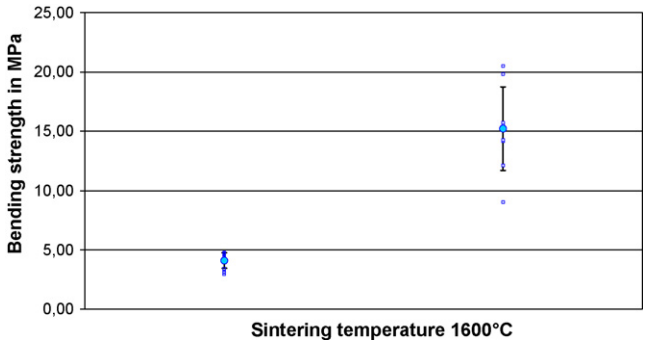


Fig. 10. Bending strengths of honeycombs (left) and rods (right) based on Material AZT 1600 sintered at 1600 °C.

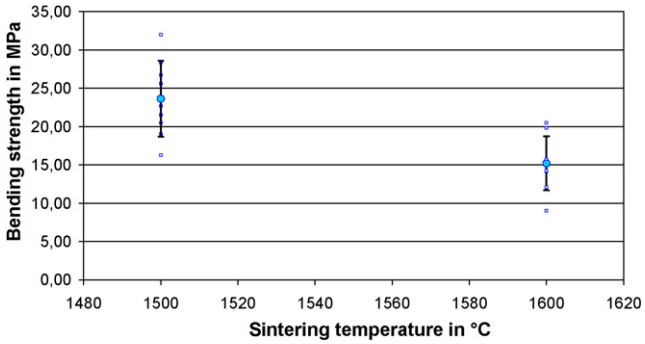


Fig. 11. Bending strengths of rods based on Materials AZT 1500 and AZT 1600 sintered at 1500 and 1600 °C, respectively.

Table 7
Mechanical properties

| | AL 1600 | AZT 1500 | AZT 1600 |
|---|---|---|---|
| $\sigma^*_{RT}$ (MPa) | | | |
| Rods | 52.2 ± 8.6 | 23.6 ± 2.6 | 15.2 ± 2.5 |
| Honeycombs | 26.7 ± 5.6 | 5.6 ± 0.3 | 4.6 ± 1.7 |
| $E_{static\,RT}$ (GPa) | | | |
| Rods | 54 ± 9.6 | 17.7 ± 7.1 | 8.5 ± 4.2 |
| Honeycombs | 28 ± 6.6 | 6.1 ± 1.5 | 4.1 ± 0.7 |

Table 8
Thermal expansion coefficients ($\alpha_{RT\text{-}1200\,°C}$ [$10^{-6}$ $K^{-1}$])

| | Rods |
|---|---|
| AL 1600 | 8.6 |
| AZT 1500 | 8.30 |
| AZT 1600 | 8.35 |

has been achieved. This low modulus of elasticity contributes to improved thermal shock performance.

Very interesting are also the results dealing with the thermal expansion. The doped materials present approximately the same value of the thermal expansion coefficient as the undoped material (Table 8). In addition in spite the fact that solid-solution areas (zones 1–3) with micro-cracks (zone 3) have been incorporated in the matrix no hysterisis of the thermal expansion curve is observed as a function of the thermal cycles. Also after the ninth thermal cycle the thermal expansion presents a linear behaviour, Fig. 12. In comparison to $Al_2TiO_5$ a hysterisis curve is always observed during heating up and down.

### 3.3. Thermal shock tests

Fig. 13 shows the geometry of special honeycomb samples (4 mm × 6 mm × 45 mm with 12 channels) for the water quenching thermal shock tests. Figs. 14 and 15 present the results of the Materials AZT 1600 and AL 1600 after water quenching thermal shock tests. Material AL 1600 loses more than 90% of its strength if it is quenched from 200 °C into water (20 °C). The residual four point bending strength of Material AZT 1600 is approximately 65% of its initial strength after quenching in water

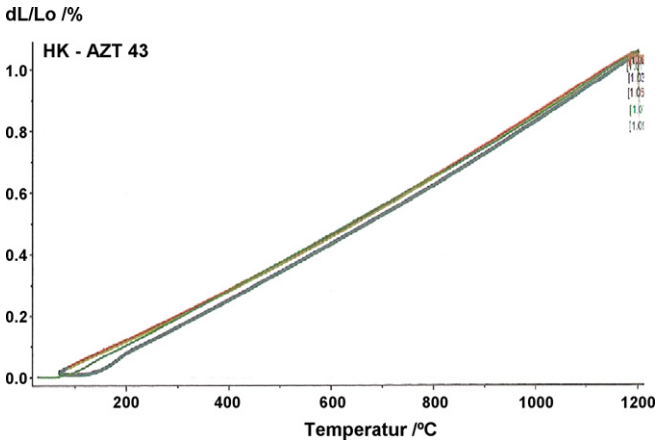


Fig. 12. Thermal expansion after nine cycles heating up to 1200 °C and cooling down at room temperature.

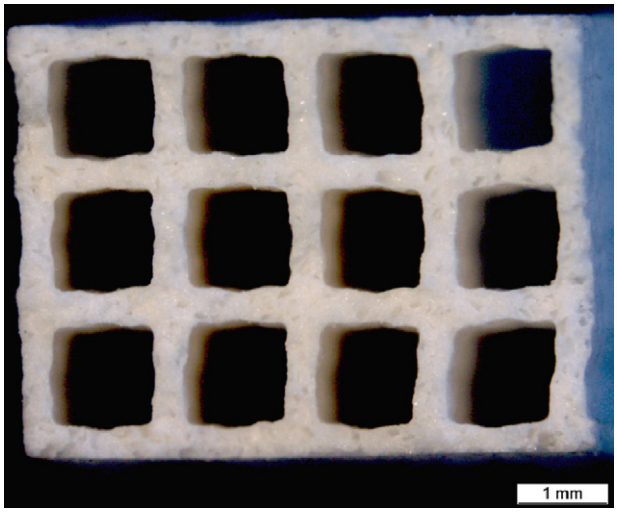


Fig. 13. Cross section of special sample geometry for water quenching tests; length of the samples 45 mm.

(20 °C) from 400 °C. In a further thermal shock test approach the honeycomb geometries as presented in Fig. 1 have been shocked for 1000 thermal cycles by heating with 800 K/min and cooling with 400 K/min, see in Fig. 16 schematic principle. Material AZT 1600 performed approximately the same residual

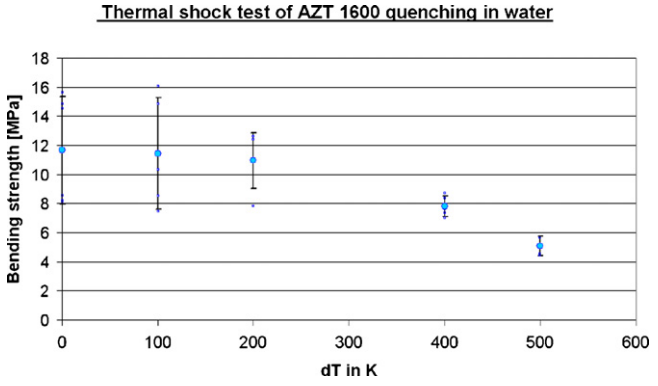


Fig. 14. Residual strengths of AZT 1600 after thermal shock test with quenching in water.

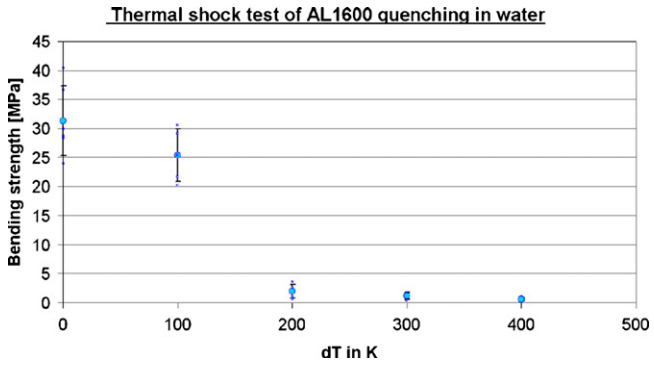


Fig. 15. Residual strengths of AL 1600 after thermal shock test with quenching in water.

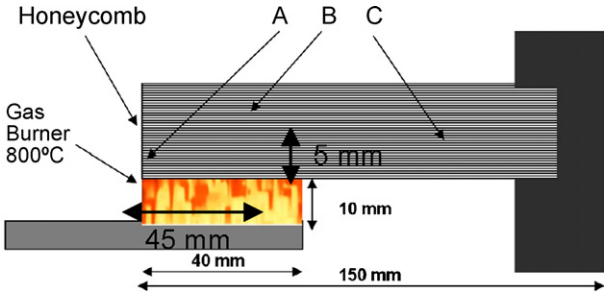


Fig. 16. Thermal shock gas burner construction (heating 800 K/min; cooling 400 K/min, thermocouples placed at positions A, B and C).

strength as its initial strength at room temperature. Material AL 1600 showed critical macro-cracks after 100 thermal cycles. No residual strengths could be measured.

Fig. 17 presents the microstructure of AZT 1600. No visible critical macro-cracks can be identified. Fig. 18 presents a magnification of Fig. 17. Monoclinic grains can be identified in the $ZrO_2$ rich area, zone 1. Further $ZrTiO_4$-precipitations due to EBSD can be registered in the $ZrO_2$-rich area. Very important is the fact, that the micro-cracks in the $ZrO_2$–$TiO_2$–$Al_2O_3$-rich area (zone 3) have remained in the same magnitude as before thermal shock attack, compare Figs. 6 and 18.

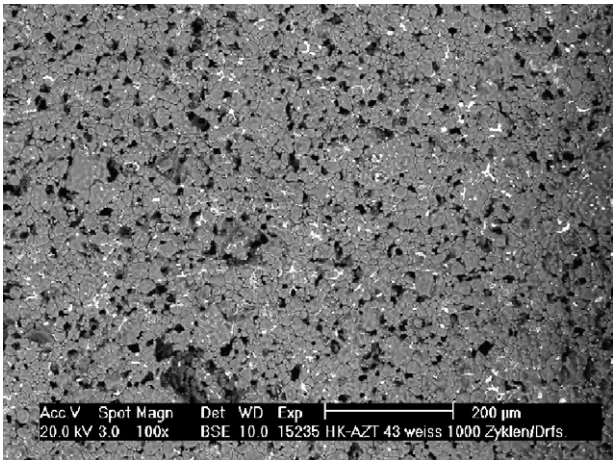


Fig. 17. Surface microstructure of AZT 1600 after 1000 thermal cycles in a special gas burner equipment, no critical cracks can be identified.

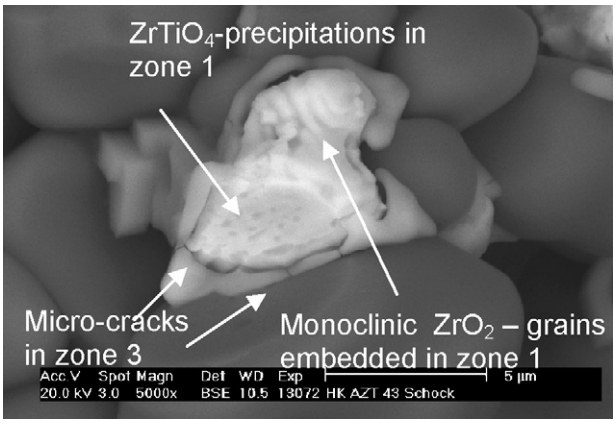


Fig. 18. Magnification of the figure, the micro-cracks in zone 3 keep the same magnitude as before the thermal shock test.

## 4. Discussion

The low Young's modulus of elasticity of the new developed fine grained porous alumina Material AZT 1600 contributes to high rupture elongations as well as to improved thermal shock performance. The rupture elongation for AZT 1600 is 0.1788%, for AZT 1500 0.0299% and for AL 1600 0.0966%.

In Fig. 19 a thermal expansion coefficient model approach is proposed in order to illustrate the effects of the different zones to the mechanical and thermo-mechanical behaviour of the composite structure of AZT 1600. In Table 9 the thermal expansion

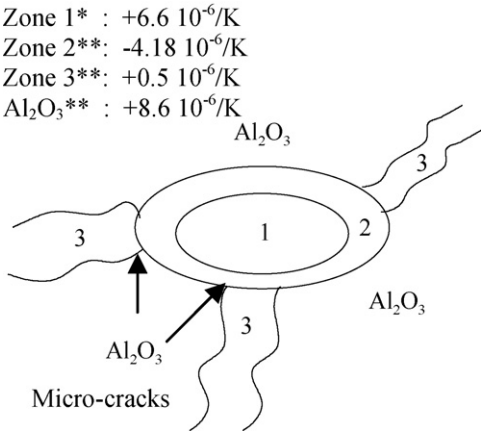


Fig. 19. Model approach for the thermo-mechanical behaviour of the microstructure of Material AZT 1600; *: data based on Aneziris et al.;[15] **: data based on Virro-Nic et al.[14]

Table 9
Thermal expansion coefficients of compositions performed by Virroo-Nic and Pilling[14]

| Material | $ZrO_2$ (mol%) | $TiO_2$ (mol%) | $Al_2O_3$ (mol%) | $\sigma$ ($10^{-6}$ $K^{-1}$) |
|---|---|---|---|---|
| $Al_2O_3$ | | | 100 | 8.6 |
| A | 65 | 20 | 15 | −0.6 |
| B | 20 | 60 | 20 | −4.18 |
| C | 40 | 40 | 20 | 0.5 |
| D | 20 | 20 | 60 | −4.1 |

coefficients of different melted composites are listed as performed by Virro-Nic and Pilling.[14] For zone 2 material B from Table 9 has been selected as an equivalent composition according to the EDX data from Table 4. For zone 3 material C also from Table 9 has been selected. Further for zone 1 a partially destabilised $ZrO_2$ material with a high amount of monoclinic phase and low thermal expansion coefficient as presented in an older work[15] has been taken under consideration for the modelling approach. Last but not least for the $Al_2O_3$-matrix a thermal expansion coefficient of $8.6 \times 10^{-6}\,K^{-1}$ has been selected.

According to Fig. 19 it is obvious that zone 1 tries to expand during heating up and zone 2 suppress zone 1 because of its negative thermal expansion coefficient. "Spring"-elements are created in the composite alumina matrix, that contribute to the high thermal shock performance during heating up as well as cooling down. In spite of the fact that micro-cracks are generated in zone 3 – that additionally contribute to the thermal shock performance – no micro-crack growth is observed after the thermal shock cycling test. The $ZrO_2$–$TiO_2$–$Al_2O_3$-rich area (zone 3) seems to be a recrystallized melt and contributes as "glue" between the $Al_2O_3$ grains and leads to a high coherence of the structure.

The very low Young's modulus of elasticity accompanied by a linear thermal expansion contribute to the thermal shock performance in spite the fact that the thermal expansion coefficient of the $Al_2O_3$-matrix remains high ($8.3 \times 10^{-6}$ K). It is assumed that the linearity of the thermal expansion, the negative thermal expansion coefficient in zone 2 in combination with the "glue" effect contribute to the stability of the micro-cracks in zone 3. In addition the Material AZT 1600 presents a non-linear mechanical behaviour with a high flexibility. This behaviour increases the performance of the material against thermal shock attacks.

By investigating further the sintering temperatures it has been registered that already above 1300 °C $TiO_2$ as well as $Al_2O_3$ diffuse in the zirconia lattice and lead to the destabilisation of zirconia. At high temperatures, although amphoteric and comparatively stable to both acid and basic oxides, zirconia can be destabilised on prolonged contact with alumino silicate compounds. The destabilisation of MgO partial stabilised zirconia is enhanced by the presence of $SiO_2$, $TiO_2$, $Fe_2O_3$ and $Al_2O_3$. It is assumed that $TiO_2$ has been incorporated in the zirconia lattice and a part of the MgO stabilising agent has been removed from the zirconia cell and has been dissolved in zone 2. Through the loss of the stabilising agent martensitic phase transformation occurs. The $Ti^{4+}$ cations, as mentioned before,[15] are not randomly incorporated in the lattice but in preferred energetic sites which cause a repulsion between the dopant cations and the vacancies. The removal of the $Mg^{2+}$ out of the lattice is followed by the energetically suitable dissolving reaction in the $TiO_2$-rich area, zone 2. The $Ti^{4+}$ as well as $Al^{3+}$ do not stabilise the zirconia. Due to the destabilisation and the transformation to the monoclinic phase volume expansion occurs that lead to new paths for incorporation of further ions in the zirconia lattice. It is very interesting that approximately 8 wt.% $TiO_2$ (a phase calculation due to the EDX quantitative identification of the Ti-element) and 2.3 wt.% $Al_2O_3$ have been identified in the $ZrO_2$-rich area. Due to the high amount of Ti-ions in the zirconia $ZrTiO_4$ precipitates are formatted at temperatures above 1500 °C in the $ZrO_2$-rich area, zone 1.

## 5. Conclusions

The improvement of the thermal shock behaviour as well as the thermal cyclic stability of fine grained porous alumina based materials have been achieved due to Mg-PSZ and $TiO_2$-additions.

Especially a 95 wt.% porous alumina material has been produced with a very good thermal shock performance that allows this material to be used in hot gas filtration applications for instance such as an alternative material for diesel soot filters. In order to achieve a very low Young's modulus of elasticity a high sintering temperature above 1500 °C is required. Due to the in situ zirconia destabilisation and the formation of a $TiO_2$-rich area with a negative thermal expansion coefficient "spring-elements" are generated in the alumina matrix.

In a future work the high chemical stability in hot gases in comparison to traditional filter materials such as silicon carbide as well as aluminium titanate will be presented.

## References


1. Freim, J., McKittrick, J., Nellis, W. J. and Katz, J. D., Development of novel microstructures in zirconia-toughened alumina using rapid solidification and shock compaction. *J. Mater. Res.*, 1996, **11**(1), 110–119.
2. Hasselman, D. P. H., Thermal stress resistance parameters for brittle refractory ceramics. *Ceram. Bull.*, 1970, **49**(12), 1033–1037.
3. Hasselman, D. P. H., Unified theory of thermal shock fracture initiation, crak propagation in brittle ceramics. *J. Am. Ceram. Soc.*, 1970, **52**(11), 600–604.
4. Aneziris, C. G., Pfaff, E. and Maier, H. R., Ceramic materials in the system $ZrO_2$–$TiO_2$–$Al_2O_3$ for applications in the ferrous and non ferrous metallurgy. *Key Eng. Mater.*, 1997, **132–136**, 1829–1833.
5. Ohya, Y. and Nakagawa, Z., Grain boundary microcracking due to thermal expansion anisotropy in aluminium titanate ceramics. *J. Am. Ceram. Soc.*, 1987, **70**(8), C184–C186.
6. Bayer, G., Thermal expansion characteristics and stability of pseudobrookitetype compounds, $M_3O_5$. *J. Less Common Met.*, 1971, **24**(2), 129.
7. Buscaglia, V. and Nanni, P., Decomposities of $Al_2TiO_5$ and $Al_{2(1-x)}$-$Mg_xTi_{(1+x)}O_5$ ceramics. *J. Am. Ceram. Soc.*, 1998, **81**(10), 2645–2653.
8. Kim, I. J. and Kwak, H. S., Thermal shock resistance and thermal expansion behaviour with composition and micorstructure of $Al_2TiO_5$ ceramics. *Can. Metall. Quar.*, 2000, **39**(4), 387–395.
9. Mchale, A. H. and Roth, R. S., Investigation of the phase transformation in $ZrTiO_4$ and $ZrTiO_4$–$SnO_2$ solid solutions. *J. Am. Ceram. Soc.*, 1983, C-18.
10. Pfaff, E., Aluminiumtitanat, *Technische Keramische Werkstoffe/ Kriegesmann J.* German Ceramic Society, 1997. ISBN 3-87156-091-X.
11. Kim, I. J. and Guozhong, C., Low thermal expansion behaviour and thermal durability of $ZrTiO_4$–$Al_2TiO_5$–$Fe_2O_3$ ceramics between 750 and 1400 °C. *J. Eur. Ceram. Soc.*, 2002, **22**, 2627–2632.
12. Pandolfelli, V. V. and Rodrigues, J. A., Effects of $TiO_2$ addition on the sintering of $ZrO_2$–$TiO_2$ compositions and on the retention of the tetragonal phase of zirconia at room temperature. *J. Mater. Sci.*, 1991, **26**, 5327–5334.
13. Osendi, M. I. and Moya, J. S., Role of titania on the sintering, microstructure and fracture toughness of $Al_2O_3$/$ZrO_2$ composites.
14. Virro-Nic, P. and Pilling, J., Thermal expansion and microstructure of melted $Al_2O_3$–$ZrO_2$–$TiO_2$ ceramics. *J. Mater. Sci.*, 1994, **13**, 950–954.
15. Aneziris, C. G., Pfaff, E. M. and Maier, H. R., Fine grained Mg-PSZ ceramics with titania and alumina or spinel additions for near net shape steel processing. *J. Eur. Ceram. Soc.*, 2000, **20**, 1729–1737.

16. Ogawa, H. and Ogasawa, T., Honeycomb ceramics, past, present and future. *Ceram. Data Book '99*, 1999, **27**, 219–224.
17. Ichikawa, Y, Yamada, S. and Yamada, T., *Development of wall flow type diesel particulate filter system with efficient reverse pulse air regeneration, SAE Paper 950735*, New York, 1995.
18. Aneziris, C. G., Walter, G., Bach, E., Schärfl, W., Strack, J. and Sandig, R., Use of microwaves for regeneration of diesel particulate filter traps, proceedings "Informationstagung Motoren". *FVV, Heft R*, 2006, **535**, 137–160.